Materials Advances

ROYAL SOCIETY OF CHEMISTRY

PAPER

View Article Online
View Journal | View Issue



Cite this: *Mater. Adv.*, 2022, 3, 2533

# Excellent microwave absorbing performance of biomass-derived activated carbon decorated with *in situ*-grown $CoFe_2O_4$ nanoparticles†

Praveen Negi,[a] Sanjeev Kumar Joshi,[b] Himangshu Bhusan Baskey,[c] Sumit Kumar,[c] Ashish Kumar Mishra[c] and Ashavani Kumar *[a]

Received 27th November 2021,
Accepted 30th January 2022

DOI: 10.1039/d1ma01116b

rsc.li/materials-advances

In this study, *in situ*-grown cobalt ferrite ($CoFe_2O_4$, CF) nanoparticles on waste biomass-derived porous activated carbon (AC) were grown *via* a facile hydrothermal technique to develop a CF/AC nanocomposite. The nanostructure and porous morphology of the nanocomposite were confirmed by FESEM, HRTEM and BET analysis. Microwave (MW) absorption analysis in the range of 2–18 GHz revealed a drastic improvement in the MW absorption performance of the CF/AC nanocomposite. Sample FAC20, having an AC loading of 20 wt%, exhibited excellent maximum reflection loss ($RL_{max}$) of −61.86 dB (@16.08 GHz) and an effective absorption bandwidth (RL < −10 dB) of 4.02 GHz at a thickness of 1.56 mm. In contrast, sample FAC30 (@30 wt% AC loading) at 1.9 mm thickness exhibited a maximum effective absorption bandwidth of 4.47 GHz in the $K_u$ band. This remarkable MW absorption performance originates from the combination of AC and CF, which results in high impedance matching followed by sufficient attenuation of microwaves. The presence of multiple interfaces and the complicated porous structure improved the interfacial polarisation, dielectric polarisation and magnetic loss ability of the CF/AC composite. Thus, the present investigation presents the CF/AC composite as an excellent biomass-based nanocomposite for MW absorption applications.



## Introduction

The swift surge in modern technology, particularly in the electronics and communication fields, has led to a large amount of electromagnetic (EM) radiation pollution, which not only impedes the proper functioning of electronic devices in civilian and military equipment but also poses a threat to human health.[1,2] Thus, significant effort has been focused on the development of novel efficient microwave (MW) absorbing materials that can be used for applications such as radar absorbing materials (RAM) for aircraft to reduce their radar cross sectional area and electromagnetic interference (EMI) shielding materials to prevent signal interference.[3,4]

A high-performance MW absorber should possess traditional properties such as strong microwave absorption and wide effective absorption bandwidth (EAB), *i.e.* a frequency bandwidth with a reflection loss (RL) of < −10 dB, and should be lightweight with low thickness and good thermal stability.[5,6] Due to their outstanding dielectric loss properties, carbon-based materials such as graphene and carbon nanotubes (CNTs) have been widely used in MW absorbing applications. They have excellent thermal stability, light weight, and superior electrical and mechanical properties,[5,7] which are essential for enhanced MW absorbers. However, their high conductivity leads to impedance mismatch, reducing their performance.[8–10] Conversely, ferrites and other magnetic materials are limited by their high density, thick coating, narrow absorption bandwidth and poor impedance matching.[2,8,11] Therefore, combining carbon-based materials with magnetic loss materials can reduce these problems and would result in better MW absorption properties, such as in the $CoFe_2O_4$ hollow sphere/graphene composite,[12] Co-doped NiZn ferrite/graphene nanocomposite,[1] $Fe_3O_4$-coated CNTs,[13] $Li_{0.3}Zn_{0.3}Co_{0.1}Fe_{2.3}O_4$@MWCNT,[14] $CoFe_2O_4$/N-doped mesoporous carbon,[15] $CoFe_2O_4$/rGO porous nanocomposite[16] and Ni/carbon foam.[17] However, these carbon-based composites have a high processing cost and are difficult to fabricate on a large scale, which limits their application.[5,8]

In recent years, activated carbon derived from biomass has shown potential as an efficient dielectric loss material.[8,18–20] The nanopores and micropores present in biomass-based

[a] *Department of Physics, National Institute of Technology Kurukshetra, Haryana 136119, India. E-mail: ashavani@yahoo.com, ashavani@nitkkr.ac.in*
[b] *Program office, Defence research and development organisation, 516 DRDO Bhawan, New Delhi 110011, India*
[c] *Defence Materials Stores Research and Development Establishment, (DMSRDE), Kanpur 208013, India*

† Electronic supplementary information (ESI) available: Particle size distribution graph with TEM images, magnetic hysteresis graph, complex permeability graph, frequency *vs.* impedance matching curves, and combined graph of RL, *Z* and thickness for FAC30. See DOI: 10.1039/d1ma01116b

activated carbon provide a blend of solid and air; thus, the material behaves as an effective medium that can facilitate better impedance matching.[18,21] Furthermore, its low density, high thermal stability, facile synthesis process and low cost make it an excellent choice for MW absorption applications.[22] The combination of biomass-derived activated carbon and magnetic loss materials has resulted in a new class of MW absorbing materials. The pine nut shell-derived activated carbon/NiO nanoflake composite synthesized by Wang *et al.* exhibited $RL_{max} = -33.8$ dB at 6 mm thickness,[23] whereas Li *et al.* synthesized porous activated carbon balls loaded with Fe, Co and Ni, which at 1.3 mm thickness gave an EAB of 3.4 GHz ($RL_{max} = -50.1$ dB), 3.8 GHz and 4.1 GHz, respectively.[24] Similarly, for coffee waste-derived bio-carbon/$MnFe_2O_4$ composites,[25] an EAB of 3.6 GHz @2.5 mm thickness and for rice husk/Fe,[7] an EAB of 5.6 GHz @1.4 mm thickness were reported.

The inclusion of cobalt in AC-based composites resulted in an improvement in their MW absorption properties, *e.g.*, the banana peel-derived porous-activated carbon/$Co_3O_4$ composite fabricated by Yusuf *et al.* exhibited $RL_{max} = -51.5$ dB and an EAB of 1.2 GHz at 2.5 mm thickness,[26] whereas the Co/$Fe_2O_3$/activated carbon synthesized by Tahir *et al.* exhibited $RL_{max} = -69.39$ dB at 4 mm thickness.[27] The biomass-derived carbon/$NiCo_2S_4$ synthesized by Hu *et al.* achieved $RL_{max} = -62.74$ dB at 2.24 mm and an excellent EAB of 7.62 GHz at 1.96 mm.[5] Thus, these results suggest the potential of activated carbon/magnetic material-based composites as MW absorbing materials. Recently, we also reported the potential of waste mango leaf biomass-based activated carbon (AC) as an excellent MW absorber.[20] When this AC was composited with another dielectric material, *i.e.*, $MoS_2$, it showed a unique dual band loss behaviour.[28]

Therefore, in the present study, cobalt ferrite (CF) nanoparticles were chosen as the magnetic loss material because of their high magnetic saturation value, Snoek's limit, chemical stability and mechanical hardness.[7,11] Subsequently, CF nanoparticles were *in situ* grown on AC to form a CF/AC composite. The MW absorption study of the CF/AC composite in the frequency range of 2 to 18 GHz demonstrated that at 20 wt% loading of AC and thickness of 1.56 mm, a wide EAB of 4.02 GHz with excellent $RL_{max} = -61.86$ dB was achieved. Herein, we report the detailed study of the enhanced MW absorption performance of the CF/AC composite.

# Experimental

## Materials

ACS grade cobalt nitrate hexahydrate and ferric nitrate nonahydrate were purchased from Lobachemie Pvt. Ltd, AR grade potassium hydroxide (KOH) was purchased from Merck Life Science Pvt. Ltd, and 25% AR grade ammonia solution, paraffin wax and hydrochloric acid (HCl) were purchased from Lobachemie Pvt. Ltd. Ethanol was purchased from Changshu Pvt. Ltd.

## Synthesis of CF/AC composite

Waste mango leaves collected from the premises our institute were used as biomass, which was carbonized and activated (using KOH) to obtain activated carbon. The detailed synthesis process has been previously reported.[20] The cobalt ferrite ($CoFe_2O_4$)/activated carbon composite was prepared *via* the hydrothermal method.[29,30] Firstly, cobalt nitrate hexahydrate and ferric nitrate nonahydrate (1 : 2 molar ratio) were dissolved in 30 mL deionized (DI) water and stirred for 1 h. Meanwhile, the desired amount of AC was added to 30 mL DI water and sonicated for 1 h. Thereafter, both solutions were mixed and stirred for 1 h, and then 25% ammonia solution was added to the solution until the pH of the mixture reached $\sim$ 9. Then 80 mL of the mixture was transferred to a Teflon-lined stainless-steel autoclave (100 mL) and kept at 180 °C for 20 h. The as-prepared precipitate was washed several times with DI water followed by ethanol under centrifugation, until the pH became neutral. The washed sample was then dried in an oven at 100 °C overnight. In all the samples, the concentration of CF was fixed, whereas the percentage loading of AC was increased, and the resulting CF/AC nanocomposites were named FAC10, FAC20 and FAC30, where the numbers 10, 20 and 30 represent the loading percentage of AC in the composite. A pure CF sample named FAC00 was also synthesized using the same procedure but without the addition of AC.

## Characterization

Powder X-ray diffraction (XRD) was performed using a Rigaku Miniflex II with Cu Kα radiation ($\lambda$ = 1.54 Å). Raman spectra were recorded using a confocal micro Raman spectrometer (AIRIX CORP) with laser excitation at 532 nm. Morphology was studied *via* field emission scanning electron microscopy (FESEM, JEOL JSM-7610F Plus) and high-resolution transmission electron microscopy (HRTEM, JEOL JEM-F200). Magnetic measurements were performed using a SQUID-VSM magnetometer (MPMS-3). A Thermo Fisher Scientific Nexsa base was used to record X-ray photoelectron spectra (XPS). A Quantachrome Novatouch LX2 was used to measure the nitrogen adsorption–desorption isotherms at 77.3 K. The multiple-point Brunauer–Emmett–Teller (BET) method was used to calculate the specific surface area and the Barrett, Joyner, Halenda (BJH) method was used to calculate the pore size distribution.

## Microwave absorption measurements

To study the microwave absorption properties, the as prepared powder samples and paraffin wax were mixed and heated at 100 °C. The mixture was then pressed into a toroidal shape ($\varphi_{out}$ = 7.0 mm and $\varphi_{in}$ = 3.0 mm) using a die. The loading of each sample in the paraffin wax was 40 wt%. An Agilent E8364B PNA series vector network analyzer (VNA) was used to obtain the relative complex permittivity ($\varepsilon_r$) and relative complex permeability ($\mu_r$) in the frequency range of 2–18 GHz. The RL values were calculated using eqn (1) and (2), as follows:[7,31]

$$RL(dB) = 20\log|(Z_{in} - Z_0)/(Z_{in} + Z_0)| \quad (1)$$

$$Z_{in} = Z_0\sqrt{\mu_r/\varepsilon_r}\tanh\left[j\frac{2\pi fd}{c}\sqrt{(\mu_r\varepsilon_r)}\right] \quad (2)$$

where $Z_{in}$ is the input impedance of the absorber, $Z_0$ is the impedance of free space, $c$ is the velocity of EM waves in free

space, $d$ is the thickness of the absorber, and $f$ is the frequency of the EM waves.

## Results and discussion

### Morphological and structural analysis

Fig. 1a depicts the XRD patterns of the CF/AC composite with different loading wt% of AC. The diffraction peaks at 18.2°, 30.09°, 35.48°, 37.3°, 43°, 53.5°, 57°, 62.6° and 74.1° represent the Braggs reflection from the (111), (220), (311), (222), (400), (422), (511), (440) and (533) planes of the cubic spinel structure of $CoFe_2O_4$ (JCPDS Card No. 22-1086), respectively.[12,32] The absence of diffraction peaks of AC in the CF/AC composite was due to the *in situ* growth of CF nanoparticles on the surface on AC, which resulted in low crystallinity in AC.[33] The intensity of the diffraction peaks was maximum for FAC00, which can be attributed to its high level of crystallinity, but as the loading of AC increased, the diffraction peak intensity showed a decreasing trend, which is due to the amorphous nature of AC.[8] Fig. 1b depicts the Raman spectra of FAC10, FAC20 and FAC30, and the bands present in the Raman spectra are listed in Table 1. The peaks present between 150 $cm^{-1}$ to 800 $cm^{-1}$ (Fig. 1c) are assigned to the five Raman active optical modes ($A_{1g} + E_g + 3T_{2g}$) present in the cubic spinel structure $Fd\bar{3}m$ space group,[34–36] showing the presence of $CoFe_2O_4$ in the CF/AC composite.[29,37] The two prominent D and G bands in the Raman spectra are the characteristic feature of graphitic carbon,[20] which substantiate the presence of AC in the CF/AC composite. The D band is attributed to the disorder and defects introduced in $sp^2$ carbon.[38,39] The G band arises due to the $E_{2g}$ vibrational mode present in aromatic carbon rings.[39] The lower $I_D/I_G$ ratio of FAC30 than that of FAC10 and FAC20 clearly suggests that a higher loading of AC in the CF/AC composite improves the degree of graphitization.[16,39]

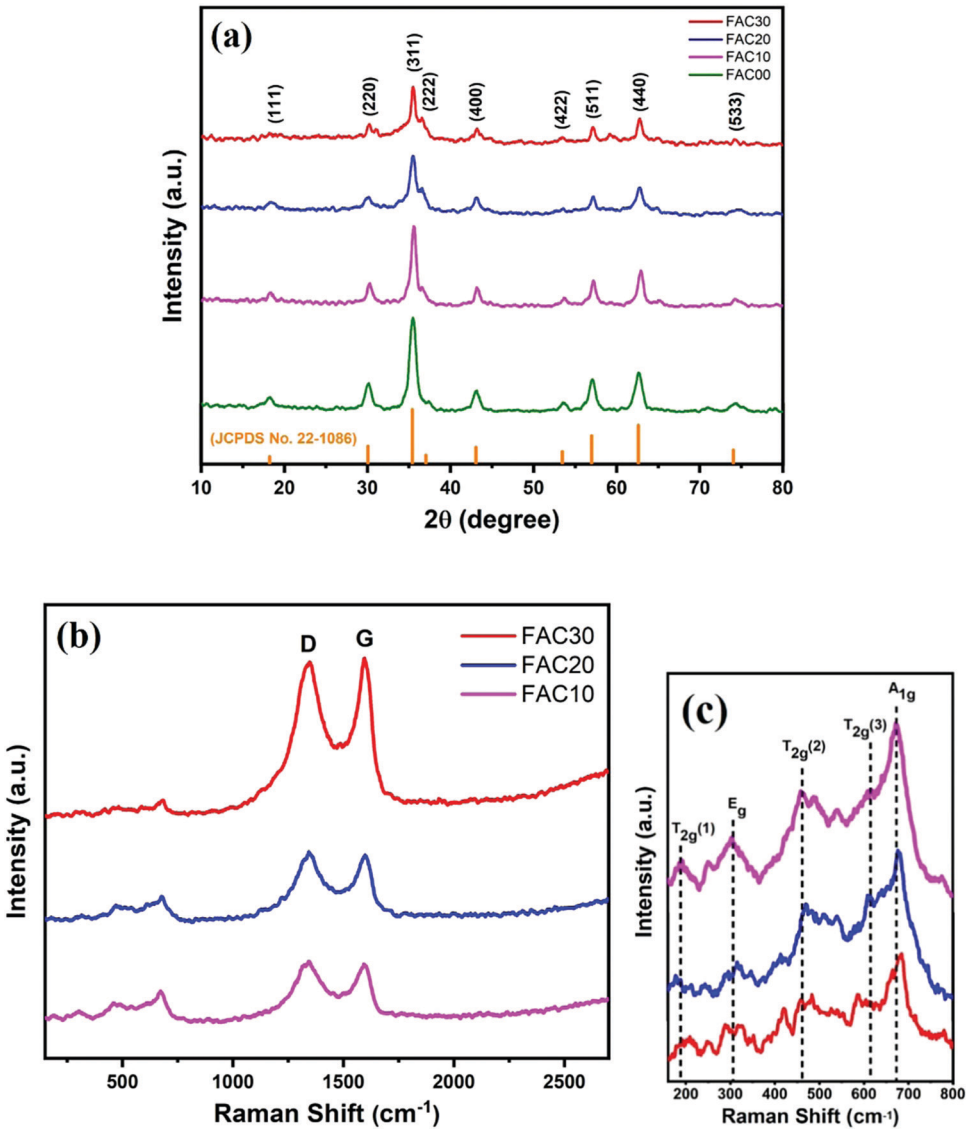


Fig. 1 (a) XRD pattern of the samples; (b and c) Raman spectra of FAC10, FAC20 and FAC30.

Table 1 Raman modes and $I_D/I_G$ ratio for the CF/AC composites

| Sample | Raman peak ($cm^{-1}$) | | | | | | | Ratio of intensity |
|---|---|---|---|---|---|---|---|---|
| | $A_{1g}$ | $E_g$ | $T_{2g}(1)$ | $T_{2g}(2)$ | $T_{2g}(3)$ | D band | G band | $I_D/I_G$ |
| FAC10 | 672 | 304 | 192 | 458 | 612 | 1341 | 1592 | 1.03 |
| FAC20 | 676 | 315 | 188 | 470 | 608 | 1343 | 1598 | 1.03 |
| FAC30 | 679 | 319 | 192 | 460 | 588 | 1346 | 1595 | 0.97 |

The FESEM image in Fig. 2a depicts the successful growth of CF nanoparticles on the surface of AC. Fig. 2b reveals the presence of pores among the uniform distribution of CF nanoparticles on AC. A higher magnification, as shown in Fig. 2(c and d), clearly shows the agglomeration of CF particles into clusters, which cover some pores but simultaneously, sufficient porosity is visible. Fig. 2d shows the amalgamation of CF nanoparticles, where the porosity of AC can be seen in greater detail. Fig. 2e and Fig. S1(a) (ESI†) depict the TEM images of the bare CF nanoparticles, which show a sphere-like morphology. In contrast, the TEM images of FAC10 (Fig. S1(b), ESI†), FAC20 (Fig. 2f) and FAC30 (Fig. 2g and Fig. S1(c), ESI†) depict the uniform distribution of CF nanoparticles on AC in the CF/AC composites. The particle size distribution graph, as shown in Fig. S1(d) (ESI†), reveals that the CF nanoparticles have a size in the range of 4 to 40 nm. The plane spacing calculated from the HRTEM image of FAC20, as depicted in Fig. 2h, is 0.48 and 0.25 nm, which correspond to the (111) and (311) planes of CF, respectively. The dashed green line represents the multiple interfaces between the CF nanoparticles, which play an important role in improving the dielectric properties of the CF/AC absorber.

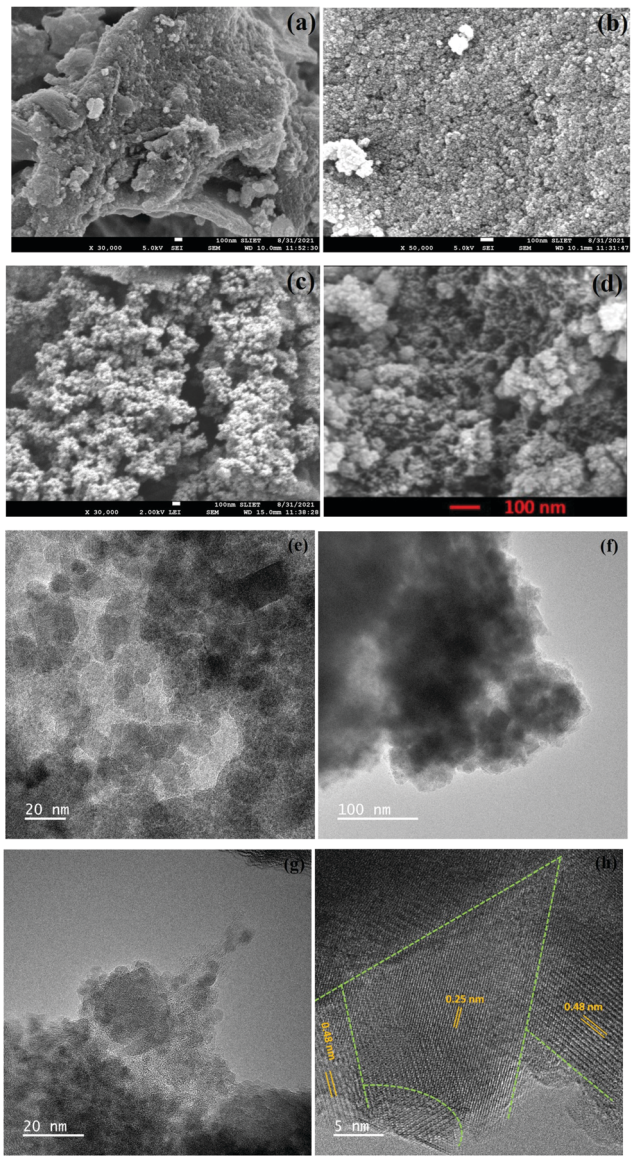


Fig. 2 (a–d) FESEM images of FAC20, TEM images of (e) FAC00, (f) FAC20 and (g) FAC30 and (h) HRTEM image of FAC20.

Further, to investigate the porosity and specific surface area of the composites, their nitrogen adsorption–desorption isotherms were measured at 77.3 K. The hysteresis curves depicted in Fig. 3(a–d) correspond to type IV isotherms for all the samples.[40–42] The specific surface area and BJH pore size distribution of the samples are presented in Table 2, where it is evident that with the incorporation of AC, the surface area of the absorber increases.

X-Ray photoelectron spectroscopy (XPS) of sample FAC20 was performed to investigate its chemical composition and oxidation states. The full XPS spectrum of the FAC20 composite shown in Fig. 4a confirms the presence of Fe, Co, C and oxygen elements.[43] Fig. 4b depicts the high-resolution spectrum of Co 2p. The two main peaks present at 781.2 and 797 eV are attributed to the Co $2p_{3/2}$ and Co $2p_{1/2}$ orbitals, respectively, and satellite peaks appear at 786.8 (Co $2p_{3/2}$) and 803.6 eV (Co $2p_{1/2}$), confirming the presence of $Co^{2+}$ in the FAC20 composite.[44–46] The two deconvoluted peaks at 780.8 and 782.8 eV can be assigned to the $Co^{2+}$ ions at the octahedral and tetrahedral sites,[47,48] respectively. The Fe 2p high-resolution spectrum of Fe 2p shown in Fig. 4c contains two peaks at 711.9 and 725.4 eV, which are attributed to the Fe $2p_{3/2}$ and Fe $2p_{1/2}$ spin orbitals, respectively.[46,49] The C 1s high-resolution spectrum, as shown in Fig. 4d, was de-convoluted into two peaks, where the dominant peak at 284.7 eV corresponds to the C–C/C=C group, whereas the smaller peak at 285.5 eV corresponds to the C–O group.[45,49]

Fig. S2 (ESI†) depicts the magnetic hysteresis loops of CF and the CF/AC composites at 300 K, which show their ferromagnetic behaviour.[44,50] The saturation magnetization ($M_s$), coercivity ($H_c$) and remanent magnetization ($M_r$) values of all the samples are reported in Table 2. The maximum $M_s$ value was obtained for the bare CF nanoparticles (FAC00), and thereafter showed a decreasing trend with an increase in the content of AC, which is due to the reduction of magnetic CF nanoparticles and increase in non-magnetic AC content in the CF/AC composite.[51]

## Microwave absorption properties

$\varepsilon_r$ and $\mu_r$ as obtained from VNA are two important parameters to study the microwave absorption properties of an absorber. $\varepsilon_r(\varepsilon_r = \varepsilon' - i\varepsilon'')$ and $\mu_r(\mu_r = \mu' - i\mu'')$ consist of two parts. The real part of permittivity, $\varepsilon'$, and real part of permeability, $\mu'$, represent

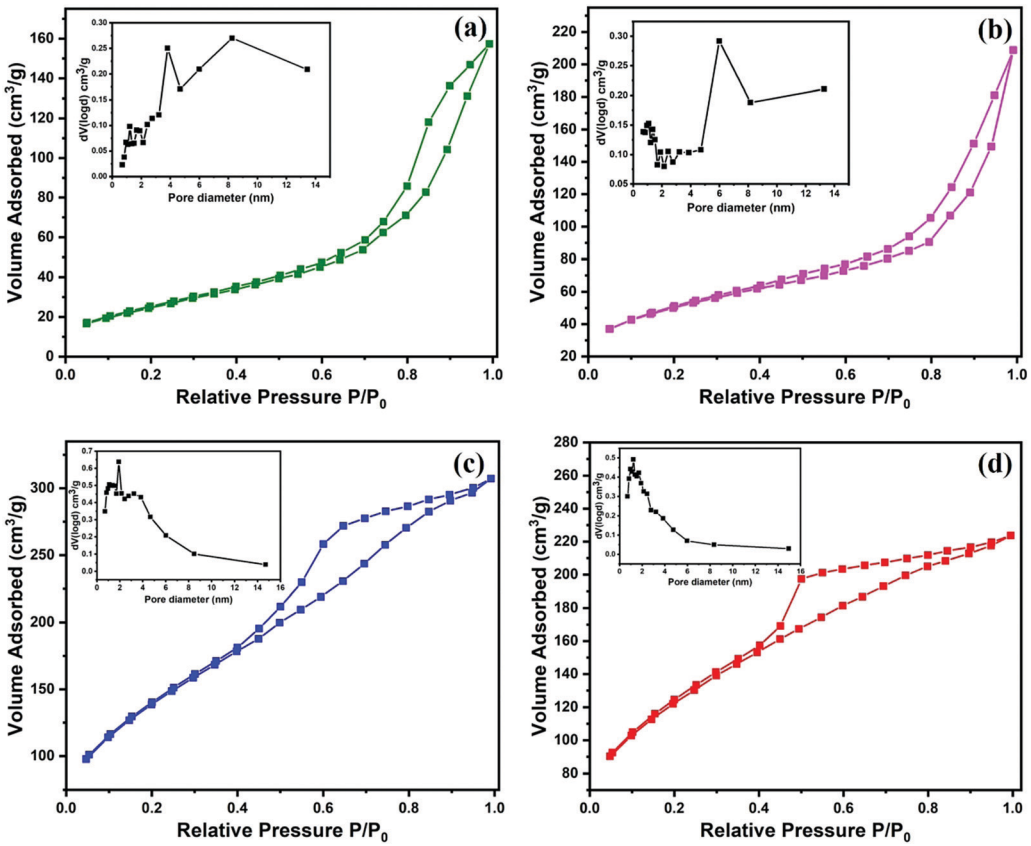


Fig. 3 Nitrogen adsorption–desorption isotherms and pore size distribution (inset) of (a) FAC00, (b) FAC10, (c) FAC20 and (d) FAC30.

Table 2 Saturation magnetization ($M_s$), coercivity ($H_c$), remanent magnetization ($M_r$), $S_{BET}$ and micropore volume (BJH) for CF and the CF/AC composites

| Sample | $M_s$ (emu g$^{-1}$) | $H_c$ (Oe) | $M_r$ (emu g$^{-1}$) | $S_{BET}$ (m$^2$ g$^{-1}$) | Micropore volume (cc g$^{-1}$) |
|---|---|---|---|---|---|
| FAC00 | 78.48 | 493 | 14.9 | 94 | 0.253 |
| FAC10 | 68.22 | 257 | 12.2 | 176 | 0.320 |
| FAC20 | 48.68 | 106 | 3.4 | 502 | 0.481 |
| FAC30 | 38.18 | 220 | 5.8 | 435 | 0.332 |

the storage of electrical and magnetic energy, respectively, whereas the imaginary part of permittivity, $\varepsilon''$, and imaginary part of permeability, $\mu''$, represent the dissipation of electrical and magnetic energy, respectively.[7,52]

For each sample, as depicted in Fig. 5a, the value of $\varepsilon'$ decreased with an increase in the frequency range, which is due to the declined response of conductance and polarization at high frequency.[53] The $\varepsilon'$ values for the FAC00, FAC10, FAC20 and FAC30 samples are in the range of 2.8 to 2.91, 3.51 to 3.84, 9.9 to 12.09 and 7.94 to 9.69, respectively. The samples FAC10, FAC20 and FAC30 showed a higher value of $\varepsilon'$ compared to the bare CF (FAC00) sample because of the addition of AC, which not only increased the conduction losses but also increased the interfacial polarization due to the formation of heterogenous interfaces between the AC and CF nanoparticles.[1,17,54] The value of $\varepsilon'$ for FAC20 is higher than that of FAC30, can be attributed to the presence of a larger number of CF nanoparticles with a 20 wt% AC loading, which not only improved the dipolar polarization but also resulted in more interfacial polarization between the CF/CF and CF/AC interfaces.[54,55] Thus, FAC20 has the optimum loading of AC to provide superior dielectric storage properties. The $\varepsilon''$ value, as depicted in Fig. 5b, is in the range of 0.08 to 0.15 for FAC00, 0.13 to 0.28 for FAC10, 2.03 to 3.05 for FAC20 and 1.68 to 3.02 for FAC30. Furthermore, a dielectric relaxation peak[55] at 14 GHz and 16.72 GHz was observed for FAC20 and FAC30, respectively.

According to the Debye theory, the imaginary permittivity can be expressed as follows:[53,56]

$$\varepsilon'' = \frac{\varepsilon_s - \varepsilon_\infty}{1 + (\omega)^2\tau^2}\omega\tau + \frac{\sigma}{\omega\varepsilon_0} = \varepsilon_p'' + \varepsilon_c'' \quad (3)$$

where $\varepsilon_s$ is the static permittivity, $\varepsilon_\infty$ is the relative dielectric permittivity at high frequency limit, $\tau$ is the relaxation time, $\omega$ is the angular frequency, $\sigma$ is the DC conductivity, and $\varepsilon_0$ is the vacuum permittivity. In eqn (3), $\varepsilon''$ consists of $\varepsilon_p''$ (polarization loss) and $\varepsilon_c''$ (conduction loss).[53] Thus, $\varepsilon_p''$ can be attributed to the relaxation peak observed in the FAC20 and FAC30 samples. The pores and defects present in AC can cause an asymmetrical charge distribution,[1,53,57] which facilitates the formation of dipoles, and thus under an EM field, the orientation of these dipoles resulted in relaxation peaks, as observed in Fig. 5b. Thus, increasing the

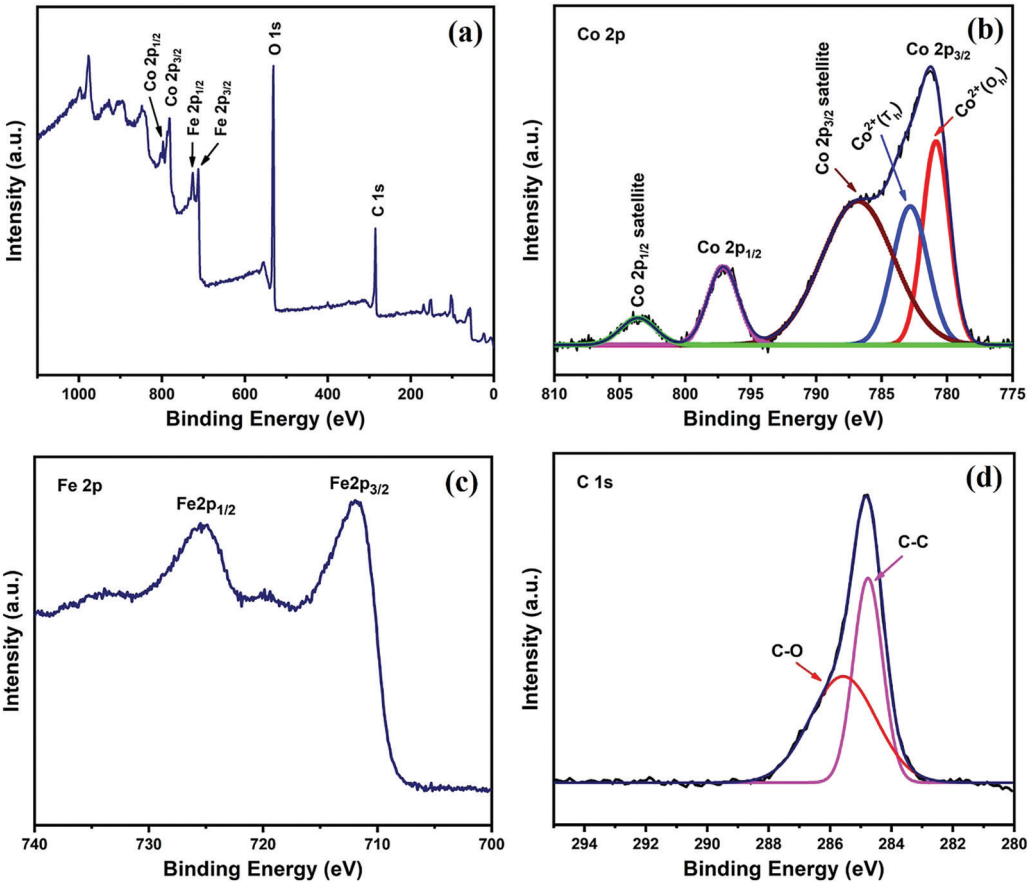


Fig. 4 (a) XPS survey spectra and high-resolution spectra of (b) Co 2p, (c) Fe 2p and (d) C 1s for FAC20.

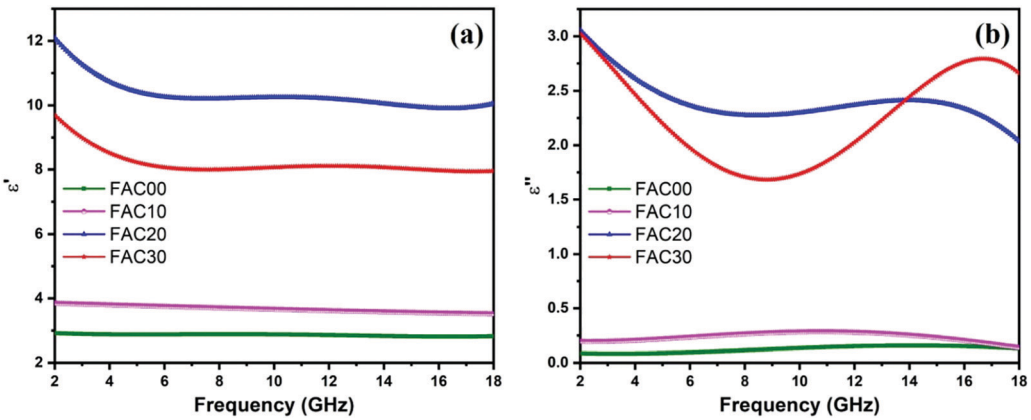


Fig. 5 Frequency dependence of the (a) real and (b) imaginary parts of relative complex permittivity for the samples.

loading percentage of AC in the absorber (FAC20 and FAC30) not only increased the conduction losses but also produced a greater amount of polarization losses. FAC30 having a higher AC loading (*i.e.*, reduced CF content) showed decreasing $\varepsilon''$ values in comparison with FAC20 in the frequency range of 2–13.9 GHz. This can be attributed to the lower number of CF/AC heterogenous interfaces, resulting in decrease dipolar and interfacial polarization losses.

According to the Debye theory, the relationship between $\varepsilon'$ and $\varepsilon''$ can be represented as follows:[38]

$$\left(\varepsilon' - \frac{\varepsilon_s + \varepsilon_\infty}{2}\right)^2 + (\varepsilon'')^2 = \left(\frac{\varepsilon_s - \varepsilon_\infty}{2}\right)^2 \quad (4)$$

The graph of the $\varepsilon'$ and $\varepsilon''$ curves depicts Cole–Cole semicircles, where each semicircle represents one Debye relaxation process.[1,31] Fig. 6(a–d) show the Cole–Cole curves of all the samples.

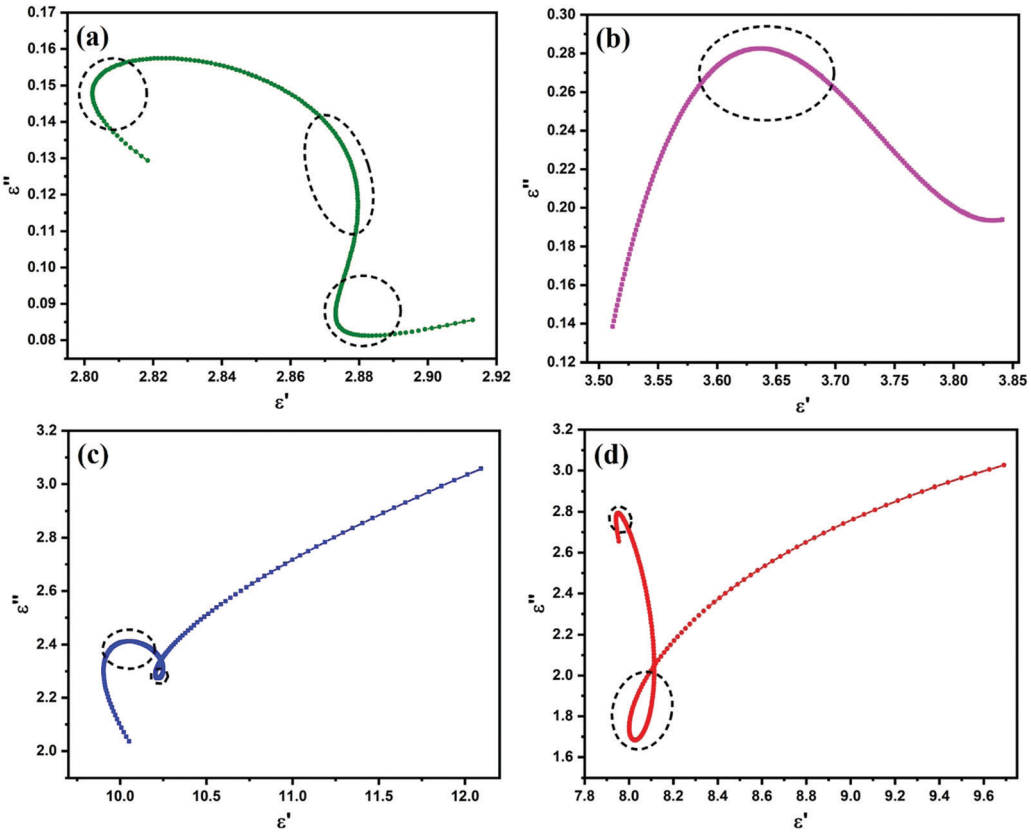


Fig. 6 Cole–Cole plots of (a) FAC00, (b) FAC10, (c) FAC20 and (d) FAC30.

The presence of semicircles in all the curves confirms their polarization loss abilities. However, for FAC10, FAC20 and FAC30, as depicted in Fig. 6(b–d), respectively, a measurable straight line depicting conduction loss[31,38] was also observed. This increase in conduction loss can be attributed to the increase in the loading of AC, which acts as a conductive path for hopping electrons.[31,53,57] Thus, due to the presence of both polarization and conduction loss, the FAC20 and FAC30 samples showed a superior dielectric loss performance among the samples (as shown in Fig. 8b).

The $\mu'$ values, as depicted in Fig. 7a, fluctuated between 0.99 to 1.02 GHz for sample FAC00, 0.97 to 1.06 GHz for FAC10, 0.90 to 1.12 GHz for FAC20 and 0.87 to 1.07 GHz for FAC30. The highest $\mu'$ values in the frequency range of 2–7.1 GHz, 7.1–12.7 GHz and 12.7–18 GHz were obtained for FAC20, FAC10 and FAC00, respectively. As shown in Fig. 7b, the $\mu''$ values fluctuated between 0.003–0.026 for FAC00, 0.036–0.090 for FAC10, 0.059–0.211 for FAC20 and 0.002–0.142 for FAC30 in the frequency range of 2 to 18 GHz. The $\mu''$ values for FAC00 initially showed a decreasing trend from 2 to 15.28 GHz, and then increased up to 18 GHz. In contrast, FAC10 displayed a broad resonance band between 2 to 15 GHz with a minor peak located at 10.7 GHz. Similarly, FAC20 and FAC30 also showed broad resonance behaviour from 2 to 15 GHz with a peak value at 9.36 GHz and 2 to 16.9 GHz with a peak value of 8.72 GHz, respectively, which correspond to multiple magnetic resonance (MMR).[58,59] The peak value of $\mu''$ was observed with a sharp decline in the $\mu'$ values in the nearby frequency range, which clearly indicates that the complex permeability of the CF/AC composites has resonance characteristics,[52,60,61] as shown in Fig. S3(b–d) (ESI†). Although there was no resonance peak observed for FAC00, as depicted in Fig. S3(a) (ESI†), this type of behaviour has also been reported by Liu *et al.*,[1] where the plausible explanation is based on the relation $H_a = 4|K_1|/3\mu_0 M_s$ and $f_r = \gamma_0 H_a/2\pi$,[1,58] where $H_a$ is the anisotropic energy, $K_1$ is the anisotropy coefficient, $\mu_0$ is the permeability in vacuum, $\gamma_0$ is the gyromagnetic ratio and $f_r$ is the resonance frequency. The high $M_s$ value of FAC00 resulted in weaker anisotropic energy, which caused the resonance frequency to be at a relatively low frequency (<2 GHz).[50] This is also evident from Fig. S3(a–d) (ESI†), where only FAC00 has a larger $\mu''$ value at 2 GHz, and then starts decreasing with an increase in frequency, whereas for all the other samples the value of $\mu''$ starts increasing from 2 GHz. With the incorporation of AC in the absorber; FAC10, FAC20 and FAC30 showed a resonance peak in the frequency range of 8 to 11 GHz. The reason for this single broad resonance peak rather than multiple resonance peaks, as reported in literature,[6,44,50] could be due to the particle size of CF. According to Fig. S1(d) (ESI†), the size of the CF nanoparticles for FAC10, FAC20 and FAC30 is between 4 to 40 nm, which is below the critical size limit under which the exchange resonance comes into effect.[58,59,62] Thus, both natural and exchange resonance resulted in this single broad resonance peak.

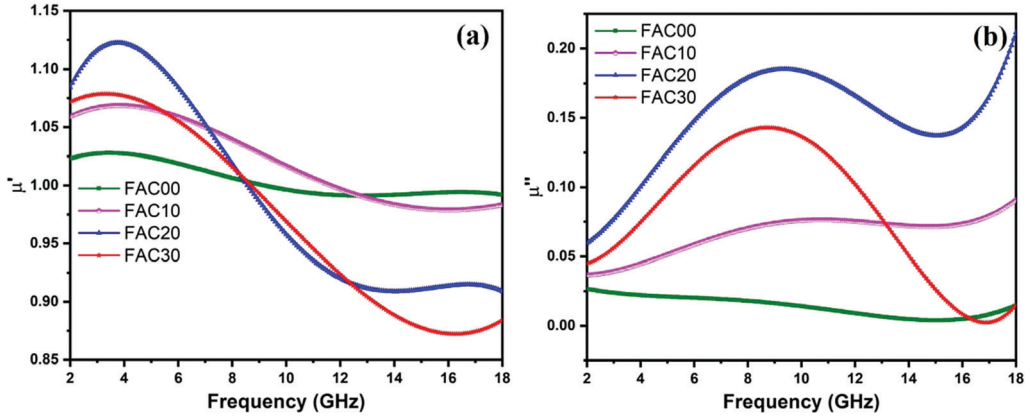


Fig. 7 Frequency dependence of the (a) real and (b) imaginary parts of relative complex permeability for the samples.

Even though activated carbon is nonmagnetic, it indirectly contributed to the enhancement in magnetic energy storage in the low frequency range of 2 to 8.4 GHz and larger magnetic energy loss in whole frequency range of 2 to 18 GHz for the CF/AC composite, except for a small range (16.32 to 17.9 GHz for FAC30, Fig. 7b). The plausible explanation for this can be related to the large surface area and pores present in AC, which resulted in the larger interaction of MW with the CF nanoparticles embedded on the surface and inside the pores in AC, where a similar type of behaviour was also reported by Wang *et al.*[63] This is evident for FAC20, which has the maximum specific surface area and the maximum values of $\mu''$ in the complete frequency range. Thus, the presence of AC in the absorber makes the CF nanoparticles more effective for magnetic energy dissipation.

The general cause of magnetic loss in magnetic materials originates from their natural resonance, domain wall resonance, hysteresis, exchange resonance and eddy current losses.[1,50,64] The domain wall resonance and hysteresis loss are negligible in the microwave frequency range,[1,65] while the

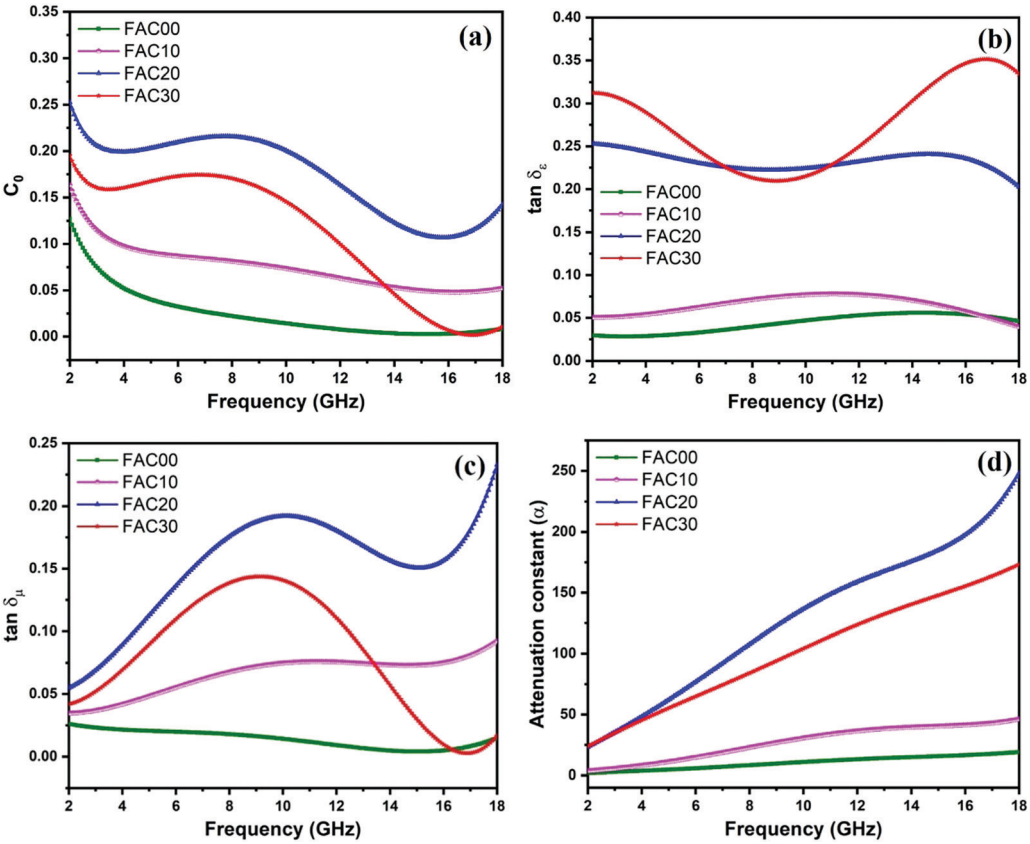


Fig. 8 (a) Frequency dependence of $C_o$, (b) dielectric loss tangent, (c) magnetic loss tangent and (d) attenuation constant (α) for all the samples.

eddy current loss can be evaluated using the following equation:[52]

$$\mu'' \approx 2\pi\mu_0(\mu')^2\sigma d^2 f/3 \quad (5)$$

where $d$ is the thickness. With an increase in frequency, if the value of $C_0(C_0 = \mu''(\mu')^{-2}f^{-1})$ remains constant, then the eddy current effect is mainly responsible for magnetic loss.[50,52,65] Given that the value of $C_0$ for all the samples (Fig. 8a) fluctuates in the entire frequency range, the eddy current loss does not have any effect on the magnetic loss mechanism. Thus, the magnetic loss mechanism is due to natural resonance and exchange resonance.[58,59,66,67]

The dielectric loss tangent [23] ($\tan\delta_\varepsilon = \varepsilon''/\varepsilon'$), as depicted in Fig. 8b, clearly shows that the dielectric loss ability of the absorber increases with an increase in the AC loading. FAC30 shows superior dielectric loss ability in the frequency range of 2 to 7.04 GHz and 10.88 to 18 GHz, whereas in the remaining frequency range of 7.04 to 10.88 GHz, FAC20 showed the highest dielectric loss ability.

Fig. 8c depicts the magnetic loss tangent[23] ($\tan\delta_\mu = \mu''/\mu'$), where it is evident that all the samples show the same trend that as of $\mu''$. The $\tan\delta_\mu$ values for FAC00 range from 0.0039 to 0.026 with minor fluctuations. In the case of FAC10, the magnetic loss dominated the dielectric loss in the higher frequency range of 13.2 to 18 GHz. FAC20 showed maximum

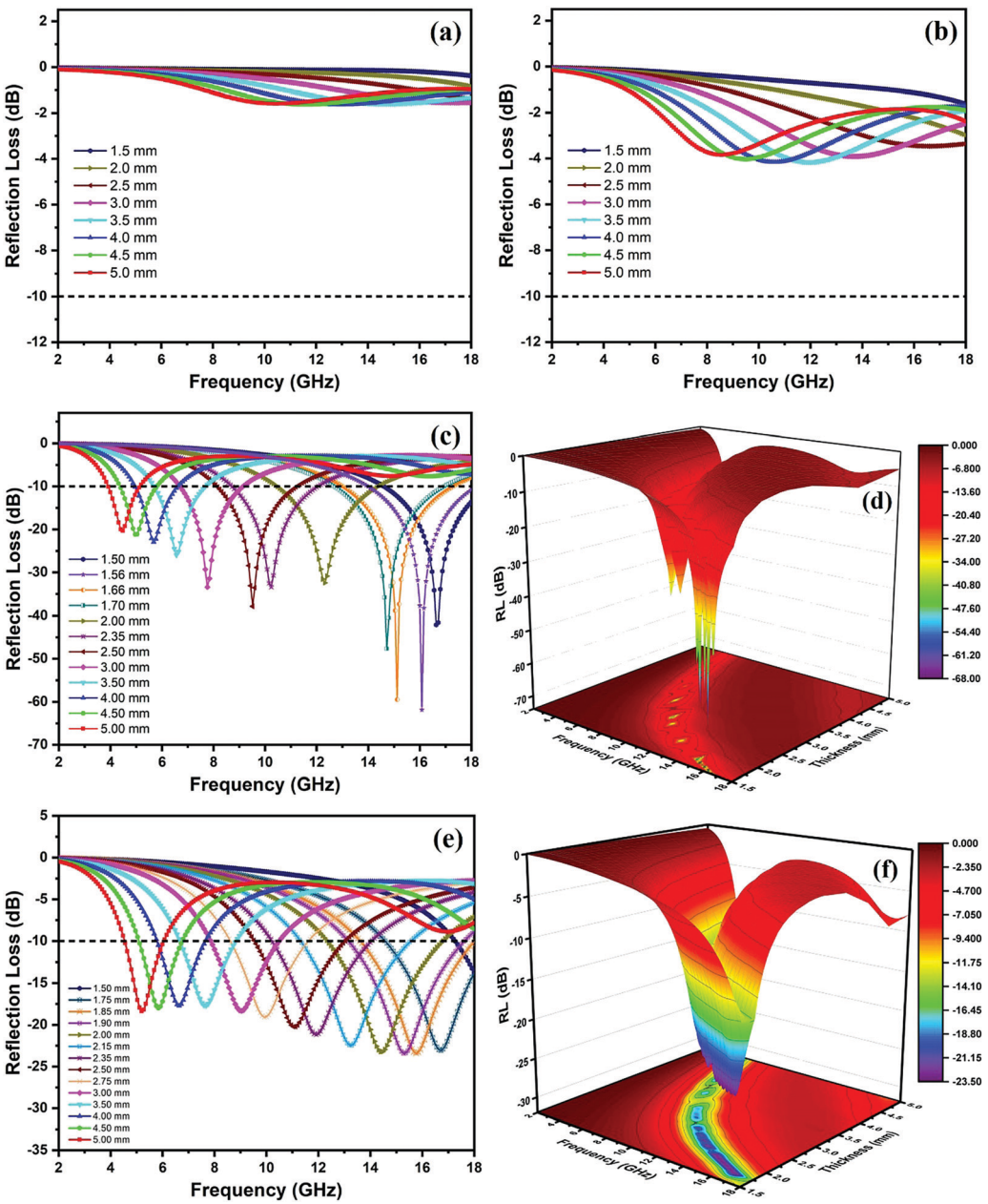


Fig. 9 Reflection loss curves of (a) FAC00, (b) FAC10, (c) FAC20 and (e) FAC30 and 3-D graph of (d) FAC20 and (f) FAC30 at thicknesses ranging from 1.5 mm to 5 mm.

tan $\delta_\mu$ values in the whole frequency range of 2 to 18 GHz with a maximum value of 0.23 at 18 GHz. The MW energy loss for FAC20 was dominated by dielectric loss in the whole frequency range except from 17.68 to 18 GHz. In contrast, for FAC30, dielectric loss dominated the complete frequency range of 2 to 18 GHz, which is due to the presence of a high concentration of AC.

The attenuation constant[38] ($\alpha$) is an important tool to understand the MW absorption mechanism of an absorber. Thus, it was calculated using eqn (6) for all the samples and is shown in Fig. 8d.

$$\alpha = \frac{\sqrt{2}\pi f}{c} \times \sqrt{(\mu''\varepsilon'' - \mu'\varepsilon') + \sqrt{(\mu''\varepsilon'' - \mu'\varepsilon')^2 + (\mu'\varepsilon'' + \mu''\varepsilon')^2}} \quad (6)$$

Although for the majority of frequency range the dielectric tangent loss value of FAC30 is greater than that of FAC20, the overall attenuation ($\alpha$) ability of FAC20 is better than that of FAC30, which is because of the higher tan $\delta_\mu$ values of FAC20 than the other samples. Thus, the synergy between both dielectric and magnetic loss resulted in enhanced MW attenuation abilities for FAC20.

Fig. S4(a–d) (ESI†) show the impedance matching ($Z$) curves for all the samples. The $Z$ was calculated using the relation $Z = |Z_{in}/Z_0|$, where $Z_0$ denotes the impedance of air. The closer the value of $Z$ closer to 1, the better the impedance matching.[7] High impedance matching is an important parameter for the enhancement in MW absorption performance.

The peak $Z$ values were in the range of 12.11 to 12.70 for FAC00, 4.39 to 5.10 for FAC10, 0.96 to 1.26 for FAC20 and 1.21 to 1.34 for FAC30. The addition of AC in the absorber significantly improved its $Z$ values. However, due to the low content of AC in FAC10, this absorber was not able to attain substantial dielectric loss ability, resulting in lower values of relative permittivity in comparison to FAC20 and FAC30, leading to its poor impedance matching performance. The incorporation of AC provides a conductive path for electrons, and according to Cao's electron hopping model,[68,69] when the path of these electrons is hindered due to defects and disorder present in AC, the electrons can hop across these barriers by absorbing the EM energy, thus maintaining a conductive network across the CF/AC composite. Higher conductivity can also lead to the surface reflection of MW, which reduces the impedance matching of the absorber, as in the case of FAC30. Overall, FAC20 exhibited the maximum impedance matching characteristics, which is due to the synergy among the conductivity, dielectric loss and magnetic loss in the AC and CF nanoparticles. Thus, these results suggest that the optimal loading of AC in the CF/AC composite is 20 wt%.

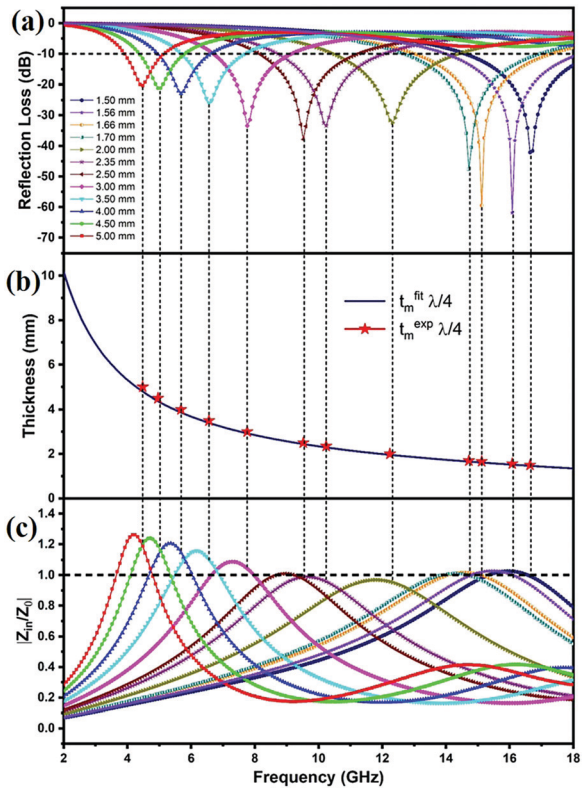


Fig. 11 (a) RL–frequency curves of FAC20 with absorber thickness ranging from 1.5 mm to 5 mm. (b) Relationship between $t_m^{fit}$, $t_m^{exp}$ and peak frequency for FAC20 under the $n\lambda/4$ model and (c) the relationship between $|Z_{in}/Z_0|$ and frequency for FAC20.

Fig. 9a depicts the RL curves for sample FAC00 at various thicknesses, where this sample exhibited a poor MW absorption performance given that all the RL values were below −2 dB. When AC was introduced with a 10 wt% loading in the absorber (FAC10), as shown in Fig. 9b, the RL values improved in

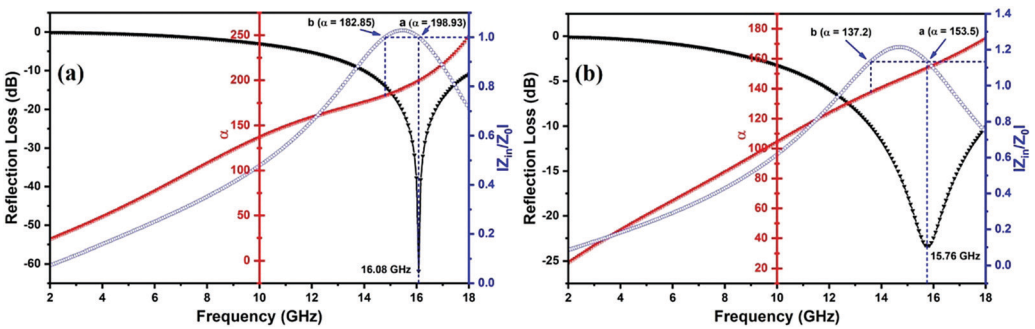


Fig. 10 Frequency dependence of RL, α and $Z$ values for (a) FAC20 and (b) FAC30.

comparison with that of FAC00, but it also failed to qualify as an MW absorbing material given that its maximum RL value was only −4.16 dB at 4 mm thickness. The reason for the poor MW absorption performance for FAC00 is the lack of conduction loss due to the absence of AC, which led to impedance mismatch and low values of dielectric losses. In contrast, for FAC10, the loading of AC improved the $Z$, $\tan\delta_\varepsilon$ and $\alpha$ values in comparison with that of FAC00, but this was still not good enough to qualify as an MW absorber.

With a further increase in AC loading to 20 wt% (FAC20), the microwave absorption performance of the absorber showed a notable enhancement. As shown in Fig. 9c (3D graph in Fig. 9d), FAC20 exhibited an excellent $RL_{max}$ = −61.86 dB at 16.08 GHz and an EAB of 4.02 GHz (13.98 to 18 GHz) at a thickness of 1.56 mm. FAC20 also gave $RL_{max}$ = −59.5 dB at 15.12 GHz and an EAB of 4.25 GHz (13.04 to 17.29 GHz) at 1.66 mm thickness, which covered 70.8% of the $K_u$ band. An EAB of 3.3 GHz (8.73 to 12.03 GHz) covering 81.75% of the X band was also obtained by FAC20 at 2.35 mm thickness with $RL_{max}$ = −33.37 (@10.24 GHz). Fig. 9(e and f) depict the RL graph and 3D graph of FAC30, respectively, which exhibited a maximum EAB of 4.47 GHz, covering 74.5% of the $K_u$ band at 1.9 mm and 2 mm thicknesses, whereas $RL_{max}$ = −23.43 dB was obtained at 15.76 GHz for 1.85 mm thickness. It is clear from the results that although the AC loading was the maximum in the FAC30 CF/AC composite, its MW absorption properties were lower compared to that of FAC20. The reason for this enhanced MW absorption performance of FAC20 can be attributed to its optimum quantity of CF and AC, which led to the maximum impedance matching and larger attenuation constant values compared to the other samples.

The impact of attenuation constant on the RL can also be realized in Fig. 10(a and b), which depict the combined graph of RL, $\alpha$ and impedance matching of FAC20 and FAC30 at 1.56 mm and 1.85 mm thickness, respectively. Points $a$ and $b$ show identical $Z$ values, as depicted in both the graphs, but the maximum RL was attained at point $a$. This is because of the larger value of $\alpha$ at point $a$.

The thickness of an absorber is also an important tool for manipulating its MW-absorbing performance. According to the quarter wavelength matching model, the relation between thickness ($t_m$) and peak frequency ($f_m$) can be expressed as follows:[44]

$$t_m = \frac{n\lambda}{4} = \frac{nc}{4f_m\sqrt{|\varepsilon_r||\mu_r|}}(n = 1, 3, 5, \ldots) \quad (7)$$

where, $c$ is the speed of light. Satisfying the above-mentioned equation at appropriate $t_m$ and $f_m$ results in a phase difference of 180° between the reflected MW from the air-absorber interface and absorber–metal interface, which leads to the cancellation of microwaves at the air–absorber interface.[7] Fig. 9(a–c and e) clearly depict that the RL peaks of all the absorbers shifted to a lower frequency with an increase in thickness, which is in accordance with eqn (7). Fig. 11(a, b) and Fig. S5(a, b) (ESI†) show the graphs of $t_m$ and $f_m$ for FAC20 and FAC30, respectively. Significantly, the red colour star denoting the experimental thickness ($t_m^{exp}$) lies directly on the $\lambda/4$ curve ($t_m^{fit}$), suggesting that both samples are in good agreement with the $n\lambda/4$ model.

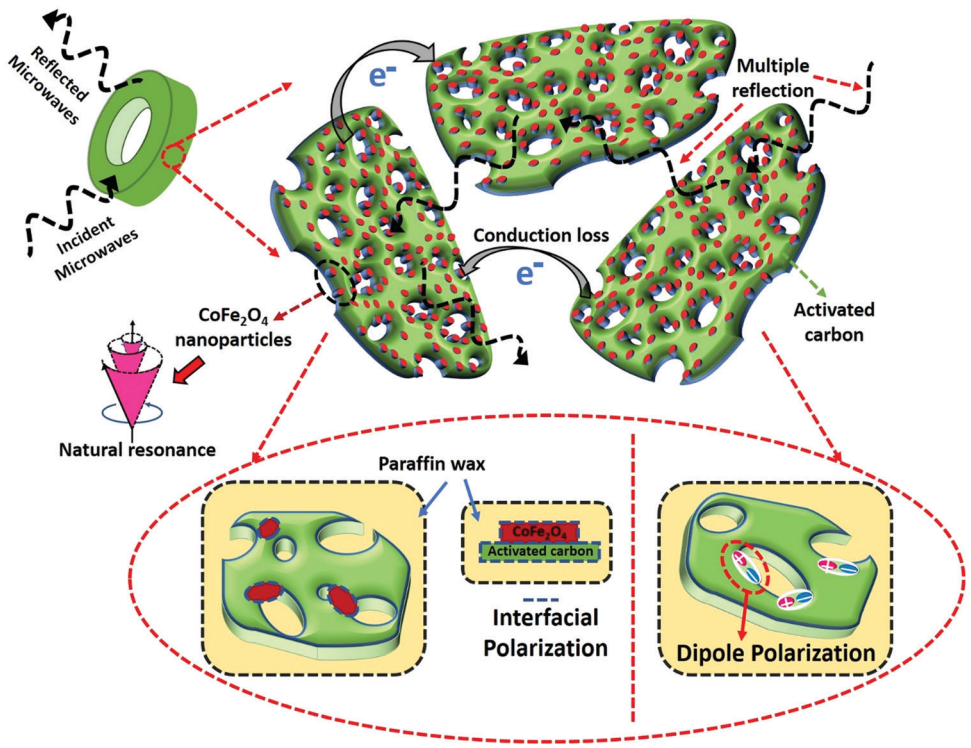


Scheme 1 Schematic illustration of the MW absorption mechanism in the CF/AC-paraffin wax composite.

Thus, an absorber can be tuned by varying its thickness according to the quarter wavelength model to achieve an enhanced MW absorbing performance in the desired frequency range.

The relationship between RL and impedance matching for FAC20 and FAC30 is shown in Fig. 11(a, c), and Fig. S5(a, c) (ESI†), respectively. The graphs clearly show that $Z$ values closer to 1 resulted in the optimal RL values. At a thickness of 1.56 mm for FAC20, the $Z$ value is $\sim$1, and hence the highest RL of −61.86 dB was obtained.

The FAC20 absorber showed the best MW absorption properties among the samples. The mechanism for this superior performance can be explained as shown in Scheme 1. Firstly, 20 wt% AC was found to be the optimum quantity in CF/AC composite, given that it resulted in the maximum impedance matching and largest surface area among the samples. The improved $Z$ values allowed a greater quantity of MW to enter the absorber, whereas the large surface area facilitated the maximum interaction of MW with the *in situ*-grown CF nanoparticles, resulting in higher dielectric and magnetic losses. The dielectric loss mechanism mainly involved (i) dipole polarizations, in which the dipoles formed at the pores and defects present in AC as well at the interface of CF/AC absorb EM energy to orient themselves along the direction of the EM field,[57,70] (ii) formation of multiple interfaces among CF nanoparticles, AC and paraffin wax, resulting in enhanced interfacial polarization, and (iii) the conduction losses due to the charge transport through the conductive network of AC[71,72] and electron hopping through the defects by absorbing EM energy. Alternatively, the magnetic loss mechanism involves the natural and exchange resonance. Therefore, the CF/AC composite is a promising material for use as an RAM material for stealth applications.

## Conclusions

Cobalt ferrite nanoparticles were successfully grown on biomass-derived activated carbon *via* a facile hydrothermal method. The large specific surface area ($S_{BET}$) of 502.02 $m^2\ g^{-1}$ for FAC20 and 434.82 $m^2\ g^{-1}$ for FAC30 suggests that even with the inclusion of CF nanoparticles, sufficient porosity was still maintained in the CF/AC composite, which is highly beneficial to enhance the MW absorption performance. The optimum loading of AC (20 wt%) with CF in FAC20 resulted in an excellent $RL_{max}$ = −61.86 dB at 16.08 GHz and EAB of 4.02 GHz, at a remarkably thin thickness of 1.56 mm. This excellent MW absorption performance of FAC20 is due to the synergistic effect of magnetic loss, dielectric and interfacial polarisation in the CF/AC absorber, thus providing better impedance matching and large attenuation ability. Therefore, this study demonstrates that CF nanoparticles incorporated with porous biomass AC (FAC20) can be a promising MW absorber for practical applications.

## Conflicts of interest

The authors declare no competing financial interest.

## Acknowledgements

Author Praveen Negi is thankful to the Director, National Institute of Technology Kurukshetra for providing Institute fellowship. We are also thankful to Director AMPRI Bhopal for the HRTEM characterization performed at analytical HRTEM laboratory, CSIR-AMPRI, Bhopal through NIT Kurukshetra and AMPRI Bhopal MOU. Authors also acknowledge Abhisek Sharma for implementing RL formulae calculation in python language.

## References

1 P. Liu, Z. Yao, J. Zhou, Z. Yang and L. B. Kong, *J. Mater. Chem. C*, 2016, **4**, 9738–9749.
2 H. Guan, H. Wang, Y. Zhang, C. Dong, G. Chen, Y. Wang and J. Xie, *Appl. Surf. Sci.*, 2018, **447**, 261–268.
3 Y. Zhao, L. Hao, X. Zhang, S. Tan, H. Li, J. Zheng and G. Ji, *Small Sci.*, 2021, 2100077.
4 F. Wang, W. Gu, J. Chen, Q. Huang, M. Han, G. Wang and G. Ji, *J. Mater. Sci. Technol.*, 2022, **105**, 92–100.
5 P. Hu, S. Dong, X. Li, J. Chen and P. Hu, *ACS Sustainable Chem. Eng.*, 2020, **8**, 10230–10241.
6 W. Liu, L. Liu, Z. Yang, J. Xu, Y. Hou and G. Ji, *ACS Appl. Mater. Interfaces*, 2018, **10**, 8965–8975.
7 J. Fang, Y. Shang, Z. Chen, W. Wei, Y. Hu, X. Yue and Z. Jiang, *J. Mater. Chem. C*, 2017, **5**, 4695–4705.
8 X. Qiu, L. Wang, H. Zhu, Y. Guan and Q. Zhang, *Nanoscale*, 2017, **9**, 7408–7418.
9 C. Wang, X. Han, P. Xu, X. Zhang, Y. Du, S. Hu, J. Wang and X. Wang, *Appl. Phys. Lett.*, 2011, **98**, 072906.
10 L. Deng and M. Han, *Appl. Phys. Lett.*, 2007, **91**, 023119.
11 Y. Yuan, S. Wei, Y. Liang, Y. Wang, B. Wang, W. Huang, W. Xin and X. Wang, *J. Magn. Magn. Mater.*, 2020, **506**, 166791.
12 M. Fu, Q. Jiao, Y. Zhao and H. Li, *J. Mater. Chem. A*, 2014, **2**, 735–744.
13 N. Li, G. W. Huang, Y. Q. Li, H. M. Xiao, Q. P. Feng, N. Hu and S. Y. Fu, *ACS Appl. Mater. Interfaces*, 2017, **9**, 2973–2983.
14 M. Dalal, J. M. Greneche, B. Satpati, T. B. Ghzaiel, F. Mazaleyrat, R. S. Ningthoujam and P. K. Chakrabarti, *ACS Appl. Mater. Interfaces*, 2017, **9**, 40831–40845.
15 G. Shen, B. Mei, H. Wu, H. Wei, X. Fang and Y. Xu, *J. Phys. Chem. C*, 2017, **121**, 3846–3853.
16 Y. Liu, Z. Chen, Y. Zhang, R. Feng, X. Chen, C. Xiong and L. Dong, *ACS Appl. Mater. Interfaces*, 2018, **10**, 13860–13868.
17 H. B. Zhao, Z. B. Fu, H. B. Chen, M. L. Zhong and C. Y. Wang, *ACS Appl. Mater. Interfaces*, 2016, **8**, 1468–1477.
18 Z. Wu, K. Tian, T. Huang, W. Hu, F. Xie, J. Wang, M. Su and L. Li, *ACS Appl. Mater. Interfaces*, 2018, **10**, 11108–11115.
19 L. Wang, P. Zhou, Y. Guo, J. Zhang, X. Qiu, Y. Guan, M. Yu, H. Zhu and Q. Zhang, *RSC Adv.*, 2019, **9**, 9718–9728.
20 P. Negi, A. K. Chhantyal, A. K. Dixit, S. Kumar and A. Kumar, *Sustainable Mater. Technol.*, 2021, **27**, e00244.
21 Q. Liu, D. Zhang and T. Fan, *Appl. Phys. Lett.*, 2008, **93**, 013110.
22 L. Liu, S. Yang, H. Hu, T. Zhang, Y. Yuan, Y. Li and X. He, *ACS Sustainable Chem. Eng.*, 2019, **7**, 1228–1238.

23 H. Wang, Y. Zhang, Q. Wang, C. Jia, P. Cai, G. Chen, C. Dong and H. Guan, *RSC Adv.*, 2019, **9**, 9126–9135.
24 G. Li, L. Wang, W. Li and Y. Xu, *ChemPhysChem*, 2015, **16**, 3458–3467.
25 A. Hassan, W. Ding, M. A. Aslam, Y. Bian, Q. Liu and Z. Sheng, *J. Mater. Res. Technol.*, 2020, **9**, 12869–12879.
26 J. Y. Yusuf, H. Soleimani, L. K. Chuan, Y. K. Sanusi and L. L. Adebayo, *J. Alloys Compd.*, 2021, **888**, 161474.
27 D. Tahir, H. Heryanto, S. Ilyas, A. N. Fahri, R. Rahmat, M. H. Rahmi, Y. Taryana and S. G. Sukaryo, *J. Alloys Compd.*, 2021, **864**, 158780.
28 P. Negi and A. Kumar, *Nanoscale Adv.*, 2021, **3**, 4196–4206.
29 A. Alazmi, V. Singaravelu, N. M. Batra, J. Smajic, M. Alyami, N. M. Khashab and P. M. F. J. Costa, *RSC Adv.*, 2019, **9**, 6299–6309.
30 A. A. Ensafi, H. A. Alinajafi, M. Jafari-Asl, B. Rezaei and F. Ghazaei, *Mater. Sci. Eng., C*, 2016, **60**, 276–284.
31 W. Gu, X. Cui, J. Zheng, J. Yu, Y. Zhao and G. Ji, *J. Mater. Sci. Technol.*, 2021, **67**, 265–272.
32 Y. Fu, H. Chen, X. Sun and X. Wang, *Appl. Catal., B*, 2012, **111–112**, 280–287.
33 Y. Wang, D. Chen, X. Yin, P. Xu, F. Wu and M. He, *ACS Appl. Mater. Interfaces*, 2015, **7**, 26226–26234.
34 S. W. Da Silva, T. F. O. Melo, M. A. G. Soler, E. C. D. Lima, M. F. Da Silva and P. C. Morais, *IEEE Trans. Magn.*, 2003, **39**, 2645–2647.
35 L. V. Gasparov, D. B. Tanner, D. B. Romero, H. Berger, G. Margaritondo and L. Forró, *Phys. Rev. B: Condens. Matter Mater. Phys.*, 2000, **62**, 7939–7944.
36 M. A. G. Soler, E. C. D. Lima, S. W. Da Silva, T. F. O. Melo, A. C. M. Pimenta, J. P. Sinnecker, R. B. Azevedo, V. K. Garg, A. C. Oliveira, M. A. Novak and P. C. Morais, *Langmuir*, 2007, **23**, 9611–9617.
37 A. Das, P. Negi, S. K. Joshi and A. Kumar, *J. Mater. Sci.: Mater. Electron.*, 2019, **30**, 19325–19334.
38 W. Gu, J. Sheng, Q. Huang, G. Wang, J. Chen and G. Ji, *Nano-Micro Lett.*, 2021, **13**, 102.
39 V. C. Tung, M. J. Allen, Y. Yang and R. B. Kaner, *Nat. Nanotechnol.*, 2009, **4**, 25–29.
40 H. Gao, L. Ding, H. Bai, A. Liu, S. Li and L. Li, *J. Mater. Chem. A*, 2016, **4**, 16490–16498.
41 Y. Lü, Y. Wang, H. Li, Y. Lin, Z. Jiang, Z. Xie, Q. Kuang and L. Zheng, *ACS Appl. Mater. Interfaces*, 2015, **7**, 13604–13611.
42 K. S. W. Sing, D. H. Everett, R. A. W. Haul, L. Moscou, R. A. Pierotti, J. Rouquerol and T. Siemieniewska, *Pure Appl. Chem.*, 1985, **57**, 603–619.
43 J. L. Ortiz-Quiñonez, U. Pal and M. S. Villanueva, *ACS Omega*, 2018, **3**, 14986–15001.
44 R. Shu, Y. Wu, Z. Li, J. Zhang, Z. Wan, Y. Liu and M. Zheng, *Compos. Sci. Technol.*, 2019, **184**, 107839.
45 R. Shu, J. Zhang, Y. Wu, Z. Wan and X. Li, *Nanoscale*, 2021, **13**, 4485–4495.
46 S. R. Naik and A. V. Salker, *J. Mater. Chem.*, 2012, **22**, 2740–2750.
47 R. S. Yadav, I. Kuřitka, J. Vilcakova, J. Havlica, L. Kalina, P. Urbánek, M. Machovsky, D. Skoda, M. Masař and M. Holek, *Ultrason. Sonochem.*, 2018, **40**, 773–783.
48 R. S. Yadav, I. Kuřitka, J. Vilcakova, J. Havlica, J. Masilko, L. Kalina, J. Tkacz, J. Švec, V. Enev and M. Hajdúchová, *Adv. Nat. Sci.: Nanosci. Nanotechnol.*, 2017, **8**, 045002.
49 X. Liu, Y. Chen, C. Hao, J. Ye, R. Yu and D. Huang, *Composites, Part A*, 2016, **89**, 40–46.
50 X. J. Zhang, G. S. Wang, W. Q. Cao, Y. Z. Wei, J. F. Liang, L. Guo and M. S. Cao, *ACS Appl. Mater. Interfaces*, 2014, **6**, 7471–7478.
51 G. Fang, C. Liu, Y. Yang, K. Peng, Y. Cao, T. Jiang, Y. Zhang and Y. Zhang, *ACS Appl. Mater. Interfaces*, 2021, **13**, 37517–37526.
52 Y. Du, W. Liu, R. Qiang, Y. Wang, X. Han, J. Ma and P. Xu, *ACS Appl. Mater. Interfaces*, 2014, **6**, 12997–13006.
53 M. Zhang, C. Han, W. Q. Cao, M. S. Cao, H. J. Yang and J. Yuan, *Nano-Micro Lett.*, 2021, **13**, 27.
54 J. Chen, J. Zheng, F. Wang, Q. Huang and G. Ji, *Carbon*, 2021, **174**, 509–517.
55 M. Ning, B. Kuang, Z. Hou, L. Wang, J. Li, Y. Zhao and H. Jin, *Appl. Surf. Sci.*, 2019, **470**, 899–907.
56 H. J. Yang, W. Q. Cao, D. Q. Zhang, T. J. Su, H. L. Shi, W. Z. Wang, J. Yuan and M. S. Cao, *ACS Appl. Mater. Interfaces*, 2015, **7**, 7073–7077.
57 X. Wang, W. Cao, M. Cao and J. Yuan, *Adv. Mater.*, 2020, **32**, 2002112.
58 J. Ma, J. Li, X. Ni, X. Zhang and J. Huang, *Appl. Phys. Lett.*, 2009, **95**, 1–4.
59 H. Wang, Y. Dai, W. Gong, D. Geng, S. Ma, D. Li, W. Liu and Z. Zhang, *Appl. Phys. Lett.*, 2013, **102**, 223113.
60 M. Zhang, H. J. Yang, Y. Li, W. Q. Cao, X. Y. Fang, J. Yuan and M. S. Cao, *Appl. Phys. Lett.*, 2019, **115**, 1–5.
61 X. X. Wang, T. Ma, J. C. Shu and M. S. Cao, *Chem. Eng. J.*, 2018, **332**, 321–330.
62 P. Toneguzzo, G. Viau, O. Acher, F. Fiévet-Vincent and F. Fiévet, *Adv. Mater.*, 1998, **10**, 1032–1035.
63 L. Wang, Y. Guan, X. Qiu, H. Zhu, S. Pan, M. Yu and Q. Zhang, *Chem. Eng. J.*, 2017, **326**, 945–955.
64 F. Wang, W. Gu, J. Chen, Y. Wu, M. Zhou, S. Tang, X. Cao, P. Zhang and G. Ji, *Nano Res.*, 2021, 1–9.
65 Y. Zhang, X. Wang and M. Cao, *Nano Res.*, 2018, **11**, 1426–1436.
66 J. Z. He, X. X. Wang, Y. L. Zhang and M. S. Cao, *J. Mater. Chem. C*, 2016, **4**, 7130–7140.
67 X. F. Zhang, P. F. Guan and X. L. Dong, *Appl. Phys. Lett.*, 2010, **96**, 1–4.
68 M. S. Cao, X. X. Wang, M. Zhang, J. C. Shu, W. Q. Cao, H. J. Yang, X. Y. Fang and J. Yuan, *Adv. Funct. Mater.*, 2019, **29**, 1807398.
69 L. Liang, W. Gu, Y. Wu, B. Zhang, G. Wang, Y. Yang and G. Ji, *Adv. Mater.*, 2021, 2106195.
70 M. Cao, X. Wang, W. Cao, X. Fang, B. Wen and J. Yuan, *Small*, 2018, **14**, 1800987.
71 X.-X. Wang, M. Zhang, J.-C. Shu, B. Wen, W.-Q. Cao and M.-S. Cao, *Carbon*, 2021, **184**, 136–145.
72 C. Han, M. Zhang, W.-Q. Cao and M.-S. Cao, *Carbon*, 2021, **171**, 953–962.